Journal of the Taiwan Institute of Chemical Engineers 158 (2024) 104750

Contents lists available at ScienceDirect

Journal of the Taiwan Institute of Chemical Engineers

journal homepage: www.journals.elsevier.com/journal-of-the-taiwan-institute-of-chemical-engineers

An Ultrastable Tetrabenzonaphthalene-Linked conjugated microporous polymer functioning as a high-performance electrode for supercapacitors

Maha Mohamed Samy [a,b], Mohamed Gamal Mohamed [a,b,*], Santosh U Sharma [c,d], Swetha V Chaganti [c,d], Jyh-Tsung Lee [c,d], Shiao-Wei Kuo [a,e,*]

[a] Department of Materials and Optoelectronic Science, College of Semiconductor and Advanced Technology Research, Center for Functional Polymers and Supramolecular Materials, National Sun Yat-Sen University, Kaohsiung 804, Taiwan
[b] Chemistry Department, Faculty of Science, Assiut University, Assiut, Egypt
[c] International PhD Program for Science, National Sun Yat-sen University, Kaohsiung 80424, Taiwan
[d] Department of Chemistry, National Sun Yat-Sen University, Kaohsiung 80424, Taiwan
[e] Department of Medicinal and Applied Chemistry, Kaohsiung Medical University, Kaohsiung 807, Taiwan

ARTICLE INFO

Keywords:
Conjugated microporous polymers
Schiff-base reaction
Tetrabenzonaphthalene
Triphenylamine
Supercapacitor

ABSTRACT

Background: Conjugated microporous polymers (CMPs) have been applied widely in several energy storage applications. Triphenylamine derivatives are good electrode materials that can be processed into SC devices because of their high charge mobilities, unique electronic properties, and high redox activity.
Methods: We prepared two novel tetrabenzonaphthalene-linked conjugated microporous polymers (TBN-pH CMPs) through [4 + 2] and [4 + 3] Schiff-base condensations of 2,7,10,15-tetra(4-formylphenyl)tetrabenzonaphthalene (TBN-PhCHO) with tetrakis(4-aminophenyl)ethene (TPE-4NH_2) and tris(4-aminophenyl)amine (TPA-3NH_2), respectively. Fourier transform infrared, and solid-state ^{13}C NMR spectroscopy investigated the structures of the as-prepared CMPs.
Significant Findings: These CMPs, had large surface areas and outstanding thermal stability at temperatures of up to 400 °C, making them suitable for use as electrodes in supercapacitor (SC) systems. Indeed, the TBN-TPA CMP–based electrode had high specific capacitances (251 F g^{-1} measured at 0.5 A g^{-1}) and capacity retentions (94%, measured after 5000 cycles at 10 A g^{-1}) when tested in three-electrode systems. We attribute the remarkable electrochemical activity and conductivity of the TBN-TPA CMP electrode to its large specific surface area (230 m^2 g^{-1}) and chemical structure featuring stacking of the benzene rings of its redox-active triphenylamine moieties.

1. Introduction

With the rapid elevation of carbon dioxide (CO_2) emissions from fossil fuels, our global societies are facing challenges relating to global warming, resource scarcity, and environmental pollution [1–4]. Great efforts are being made to decrease CO_2 emissions through the development of inexpensive eco-friendly devices that should provide sustainable benefits to our communities [5,6]. For example, functional, reliable, and flexible electrochemical energy storage (EES) systems, including lithium-ion batteries, water-splitting electrolyzers, and supercapacitors (SCs), are becoming increasingly popular for powering emerging electronic devices. In particular, SCs [also known as electrical-double-layer capacitors (EDLCs)] are being employed in supplementary emergency power systems, energy recovery systems, smart grids, new energy vehicles, and high power supplies, owing to their very long cycle lives, ultrahigh power densities, exemplary rate capabilities, broad operating temperature ranges, ultrahigh charging/discharging rates, and outstanding reversibility; they also have great potential to accommodate growing power demands [7–12]. Nevertheless, the energy densities achieved by SCs remain low when compared with those of other rechargeable batteries; furthermore, SCs occupy only a small sector of the market for EES devices [13,14]. Great efforts are being made, however, to enhance the energy densities of SCs and create materials with multifunctional characteristics (i.e., large surface areas, tunable porous structures, highly conductive networks, and wettability) so that the utility of SC devices can be extended [15,16]. Conjugated polymers

* Corresponding authors.
E-mail addresses: mgamal.eldin12@aun.edu.eg (M.G. Mohamed), kuosw@faculty.nsysu.edu.tw (S.-W. Kuo).

https://doi.org/10.1016/j.jtice.2023.104750
Received 23 September 2022; Received in revised form 12 February 2023; Accepted 12 February 2023
Available online 18 February 2023

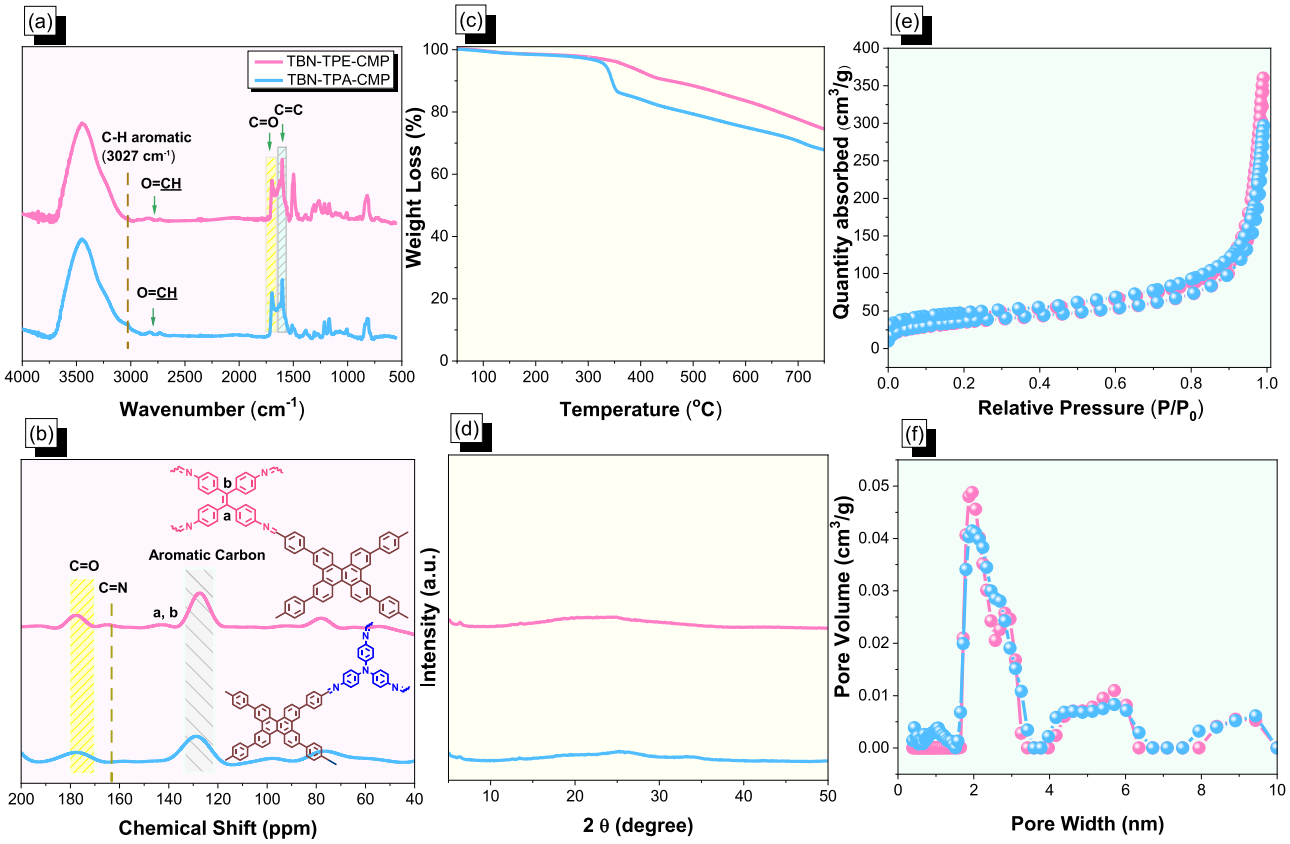

Fig. 1. (a) FTIR spectra, (b) solid-state ^{13}C NMR spectra, (c) TGA traces, (d) XRD patterns, (e) N_2 sorption isotherms, and (f) PSD profiles of the TBN-TPE and TBN-TPA CMPs.

are often employed in SC devices, in part because they are inexpensive and abundant. For example, polyaniline nanostructures offer a capacitance of 1221 F g^{-1} when applied as electrode materials; this value is much higher than the specific capacitances provided by activated carbon electrodes (<200 F g^{-1}) [17,18]. Nevertheless, classical conjugated polymers (e.g., polypyrrole, polythiophene, and polyaniline) are usually nonporous and not sufficiently durable; they generally experience degradation after being subjected to charge/discharge cycles, due to shrinkage and swelling of their mostly linear macromolecular components [19]. Because they feature expanded π-conjugated sequences within nanoporous polymer networks, conjugated microporous polymers (CMPs) are an emerging class of porous organic polymers (POPs) with great potential for use in SCs [20–23]. CMPs have typically been constructed using C–N or C–C coupling reactions (e.g., Buchwald–Hartwig amination, Schiff base formation, cyclotrimerization, phenazine ring fusion, Yamamoto coupling, Suzuki–Miyaura coupling, Sonogashira–Hagihara coupling, and oxidative polymerization) [24–30]. The resulting CMPs have been tested for use in a plethora of applications, including energy storage, energy conversion, catalysis, chemosensing, gas separation and storage, light-emitting diodes, and various biological fields [31–45]. Owing to the numerous building blocks of CMPs structures, the ability to vary their π-conjugated units, and their ready structural tunability, CMPs are in many ways better than traditional electrode materials when designing SC electrodes [46–50]. Herein, we describe two novel CMP networks formed through facile Schiff-base condensations of 2,7,10,15-tetra(4-formylphenyl)tetrabenzonaphthalene (TBN-PhCHO) with the amino monomers tetrakis (4-aminophenyl)ethene (TPE-4NH_2) and tris(4-aminophenyl)amine (TPA-3NH_2). These CMP materials possessed good porosities and outstanding redox activities, making them appropriate electrode materials for three-electrode and symmetrical SC (SSC) devices.

2. Experimental part

2.1. Materials

Potassium carbonate (K_2CO_3), anhydrous magnesium sulfate ($MgSO_4$), charcoal, 10% Pd/C, 4,4′-diaminobenzophenone, 4-formylphenylboronic acid (PhB-CHO), acetic acid (AcOH), and sodium hydroxide (NaOH) were purchased from Sigma–Aldrich. Hydrazine monohydrate, mesitylene, 1,4-dioxane (DO), tetrahydrofuran (THF), and acetone were obtained from Alfa Aesar. Tetrabromotetrabenzonaphthalene (TBN-Br_4) was prepared according to our previous reported [4].

2.2. 2,7,10,15-Tetra(4-formylphenyl)tetrabenzonaphthalene (TBN-PhCHO)

$Pd(PPh_3)_4$ (0.1 g, 0.08 mmol) and K_2CO_3 (0.88 g, 6.34 mmol) were placed in the two-neck round-bottom flask (250 mL) containing TBN-Br_4 (0.510 g, 0.790 mmol) and PhB-CHO (0.712 g, 0.4.80 mmol) and then the system was degassed three times through pumping with N_2. Then, 1,4-dioxane (DO, 80 mL) was added, and the mixture was heated at 100 °C for 48 h. After that, ice/cold water was added, followed by HCl (2 mL) to dissolve any potassium carbonate that remained. The crude yellow product was heated under reflux in MeOH (35 mL) for 45 min to remove any residual reactants. TBN-PhCHO was obtained as a yellow solid after filtration and drying in an oven (Scheme S1). FTIR (Fig. S1): 2824, 2734 (CH═O), 1690, 1603. ^1H NMR (DMSO-d_6, δ, ppm, Fig. S2): 10.073 (4H, CH═O), 8.060–7.738 (aromatic CH). ^{13}C NMR (DMSO-d_6, δ, ppm, Fig. S3): 192.72, 144.28, 135.81, 135.09, 134.43, 134.43, 130.29, 130.14, 128.27, 127.82, 127.15, 115.74.

Table 1
TGA as well as BET results of TBN-TPE and TBN-TPA CMPs.

Sample	T_{d5} (°C)	T_{d10} (°C)	Char yield (wt%)	Surface area ($m^2\ g^{-1}$)	Pore size (nm)
TBN-TPE CMP	372	457	73	126	1.96
TBN-TPA CMP	332	346	66	230	1.99

2.3. Tetrakis(4-aminophenyl)ethene (TPE-4NH_2) [51]

HCl (45 mL) was added to 4,4′-diaminobenzophenone (0.950 g, 4.27 mmol) at 65 °C under N_2. Sn (2.85 g, 23.8 mmol) was added slowly into the mixture, which was then kept at 70 °C for 20 h. The flask was cooled, and the solid was washed with water, MeOH, and 1 N NaOH. TPE-4NH_2 was obtained as a green powder after drying in an oven for 24 h at 55 °C (Scheme S2). FTIR (KBr, cm^{-1}, Fig. S4): 3421, 3357 (N–H), 3027 (aromatic C–H), 1520 (C = C). ^{1}H NMR [DMSO-d_6, δ, ppm, Fig. S5(a)]: 6.58 (8H), 6.28 (8H), 4.84 (8H, NH_2). ^{13}C NMR [DMSO-d_6, δ, ppm, Fig. S5 (a)]: 146, 136.7, 132.8, 131.6, 113.1.

2.4. Tris(4-aminophenyl)amine (TPA-3NH_2) [52]

TPA-3NO_2 (6.60 g, 17.36 mmol) was dissolved in DO (50 mL), then 10% of Pd/C powder (0.43 g, 4.04 mmol) was mixed, and then the mixture was heated at 90 °C. After 2 h, hydrazine hydrate (17.9 g, 394 mmol) was added dropwise, and then heating the mixture was continued for two days. After cooling to room temperature, charcoal was added, and the solids were filtered off. The filtrate was mixed with ice for 1 h to give a green precipitate. TPA-3NH_2 was collected through filtration (Scheme S3). FTIR (KBr, cm^{-1}, Fig. S6): 3407 and 3335 (N–H). ^{1}H NMR [DMSO-d_6, δ, ppm, Fig. S7(a)]: 6.70–6.38 (aromatic C–H), 4.68 (s, 4H, NH_2). ^{13}C NMR [DMSO-d_6, δ, ppm, Fig. S7(a)]: 143.18–114.80 (aromatic carbon nuclei).

2.5. TBN-TPE and TBN-TPA CMPs

TBN-PhCHO (0.050 g, 0.067 mmol), TPE-4NH_2 (0.026 g, 0.066 mmol), and AcOH (6 M, 1 mL) were mixed together in mesitylene/DO (1:1, 10 mL) in a Pyrex tube (25 mL). The mixture was frozen using liquid N_2 (at 77 K) and degassed through three freeze/pump/thaw cycles, and then the tube was closed under the vacuum of an oil pump. After three days of heating the tube at 110 ℃, the tube was cooled, and the resulting solid was gained by filtration and then washed three times

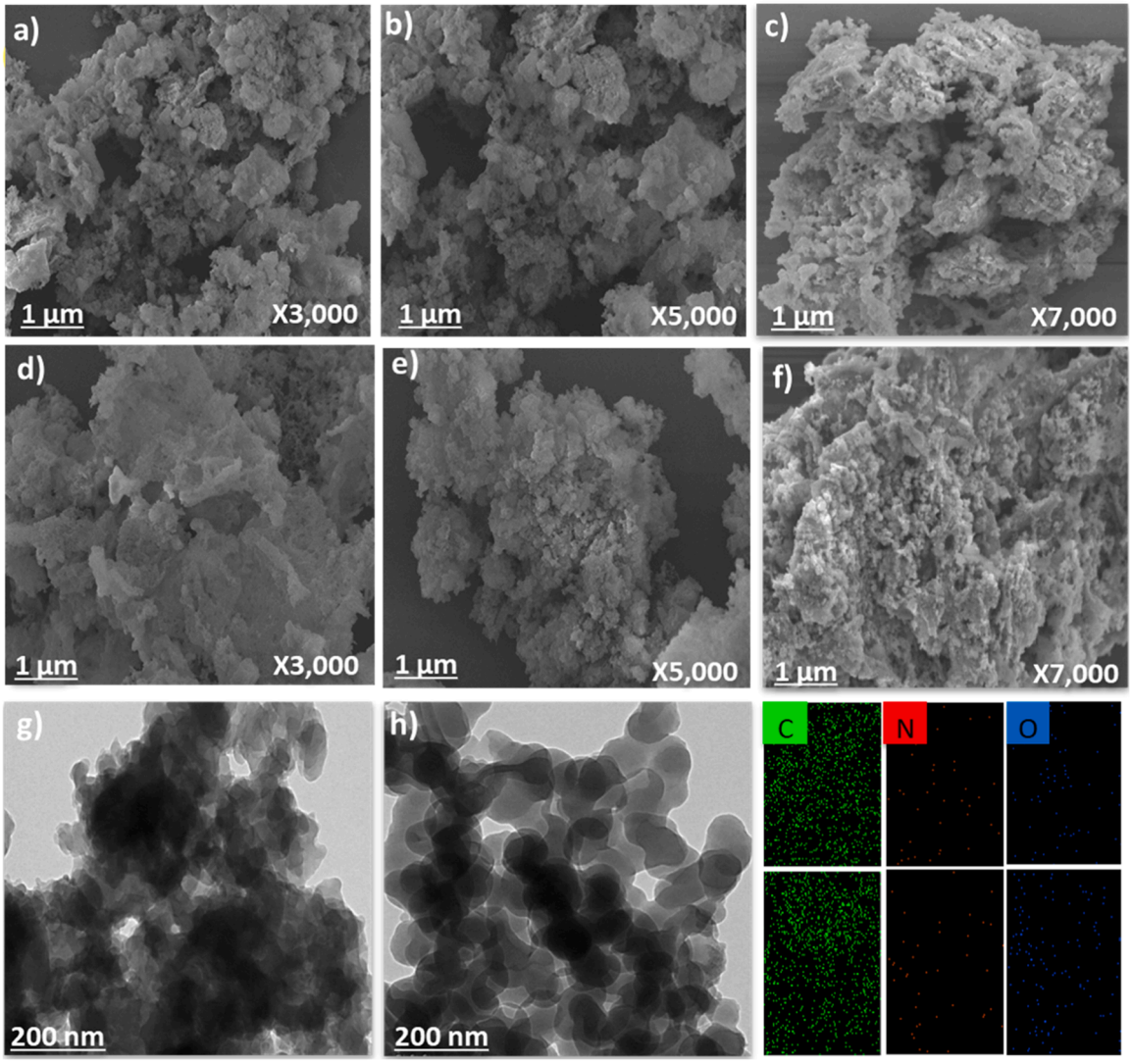

Fig. 2. (a–f) SEM images of the (a–c) TBN-TPE and (d–f) TBN-TPA CMPs, presented at various magnifications. (g, h) TEM images of the (g) TBN-TPE and (h) TBN-TPA CMPs and their EDS elemental maps for C, N, and O atoms.

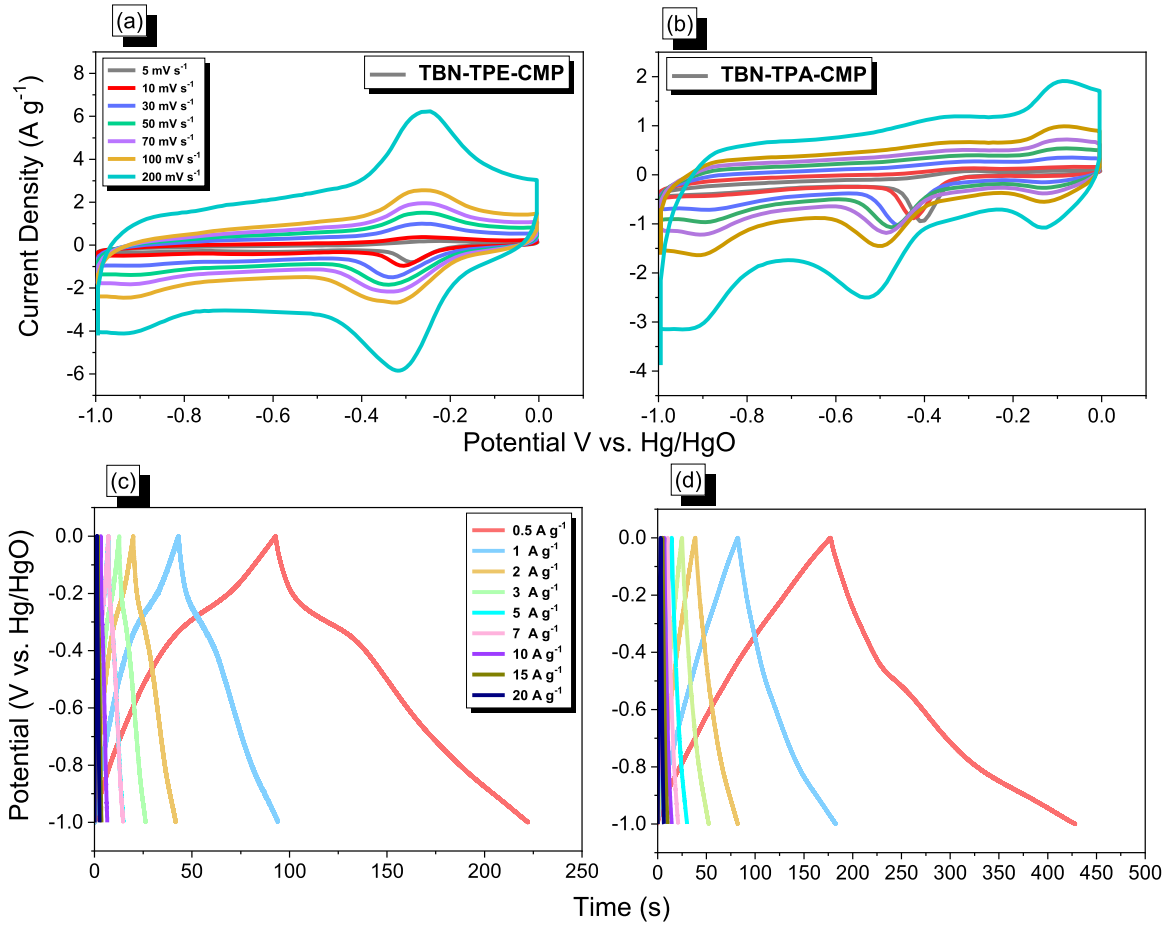

Fig. 3. (a, b) CV and (c, d) GCD curves of the (a, c) TBN-TPE and (b, d) TBN-TPA CMPs.

with THF, MeOH, and acetone. TBN-TPECMP was obtained as a green powder after drying at 70 °C overnight under a vacuum (Scheme 1). Employing the same method, but using TPA-3NH_2 (0,026 g, 0.089 mmol) in place of TPE-4NH_2, TBN-TPA CMP was afforded as a gray powder (Scheme 1). FTIR [KBr, cm^{-1}, Fig. 1(a)]: 2828, 2739 (CH═O), 1697 (C = O).

3. Results and discussion

We prepared the novel imine-linked TBN-TPE and TBN-TPA CMPs through Schiff-base condensations of TBN-PhCHO with the amino monomers TPE-4NH_2 and TPA-3NH_2, respectively, in a mixture of mesitylene, DO, and 6 M AcOH at 110 °C for three days (Scheme 1). We synthesized the precursors TBN-PhCHO, TPE-4NH_2, and TPA-3NH_2 in good yields by using previously reported procedures (Schemes S1–S3). The Fourier transform infrared (FTIR) spectrum (Fig. S1) of the TBN-PhCHO monomer featured three significant bands at 2824, 2734 (CH═O), and 1696 (C = O) cm^{-1}, consistent with the presence of aldehyde groups, as confirmed by the ^{1}H NMR spectrum containing a signal at 10.06 ppm (Fig. S2). For the TPE-4NH_2 and TPA-3NH_2 monomers, the FTIR spectra (Figs. S4 and **S6**) displayed absorption bands at 3421 and 3357 cm^{-1} for TPE-4NH_2 and at 3407 and 3335 cm^{-1} for TPA-3NH_2, representing N–H stretching of the amino groups. The presence of amino groups in TPE-4NH_2 and TPA-3NH_2 was confirmed through the appearance of signals at 4.84 and 4.68 ppm, respectively, based on ^{1}H NMR data [Figs. S5(A) and S7(A)]. The solubility test revealed that TBN-TPE and TBN-TPA CMPs are insoluble in most organic solvents [Fig. S8]. We characterized our imine-linked CMPs using FTIR and solid-state ^{13}C NMR spectroscopy. The FTIR spectra of both CMPs both featured intense signals at 1618 and 1601 cm^{-1}, representing their imino (C = N) and aromatic (C = C) units, as well as attenuated bands centered at 2828, 2739, and 1697 cm^{-1}, attributable to remaining terminal formyl groups [Fig. 1(a)]. The solid-state ^{13}C NMR spectra of the TBN-TPE and TBN-TPA CMPs both featured a signal near 163 ppm, representing the carbon nuclei of C = N groups, confirming the presence of imino linkers. In addition, signals appeared at 178 ppm and in the range 118–135 ppm, representing the terminal formyl units and the aromatic carbon nuclei, respectively. Furthermore, a significant signal was evident near 143 ppm in the spectrum of the TBN-TPE CMP, representing the C = C groups in the tetraphenylethylene units [Fig. 1(b)]. As can be seen in FTIR results [Figs. S9 and S10], both TBN-TPE and TBN-TPA CMPs have excellent chemical stability in organic solvents. Next, we used thermogravimetric analysis (TGA) under N_2 air to examine the thermal stabilities of our imine-linked CMPs. The TGA traces of both samples revealed high 5 and 10 wt% decomposition temperatures (T_{d5} and T_{d10}, respectively) and large residual weights. For the TBN-TPE CMP, the values of T_{d5} and T_{d10} were 372 and 457 °C, respectively, and the residual weight was 73 wt%; for the TBN-TPA CMP, these values were 332 and 346 °C and 66 wt%, respectively [Fig. 1(c) and Table 1]. Powder X-ray diffraction (PXRD) analyses revealed amorphous nature for both the TBN-TPE and TBN-TPA CMPs, confirming their amorphous nature [Fig. 1(d)]. To investigate the porosities of our CMPs, we performed N_2 sorption measurements at 77 K. The TBN-TPE and TBN-TPA CMPs both provided type III isotherms, with Brunauer–Emmett–Teller (BET) surface areas (S_{BET}) of 126 and 230 m^2 g^{-1}, respectively [Fig. 1(e)]. We applied non-local density functional theory to evaluate the pore size of our two CMPs. The pore size distribution (PSD) profiles of the TBN-TPE and TBN-TPA CMPs revealed average pore widths of 1.96 and 1.99 nm, respectively [Fig. 1(f)].

Fig. 2 presents scanning electron microscopy (SEM) and transmission

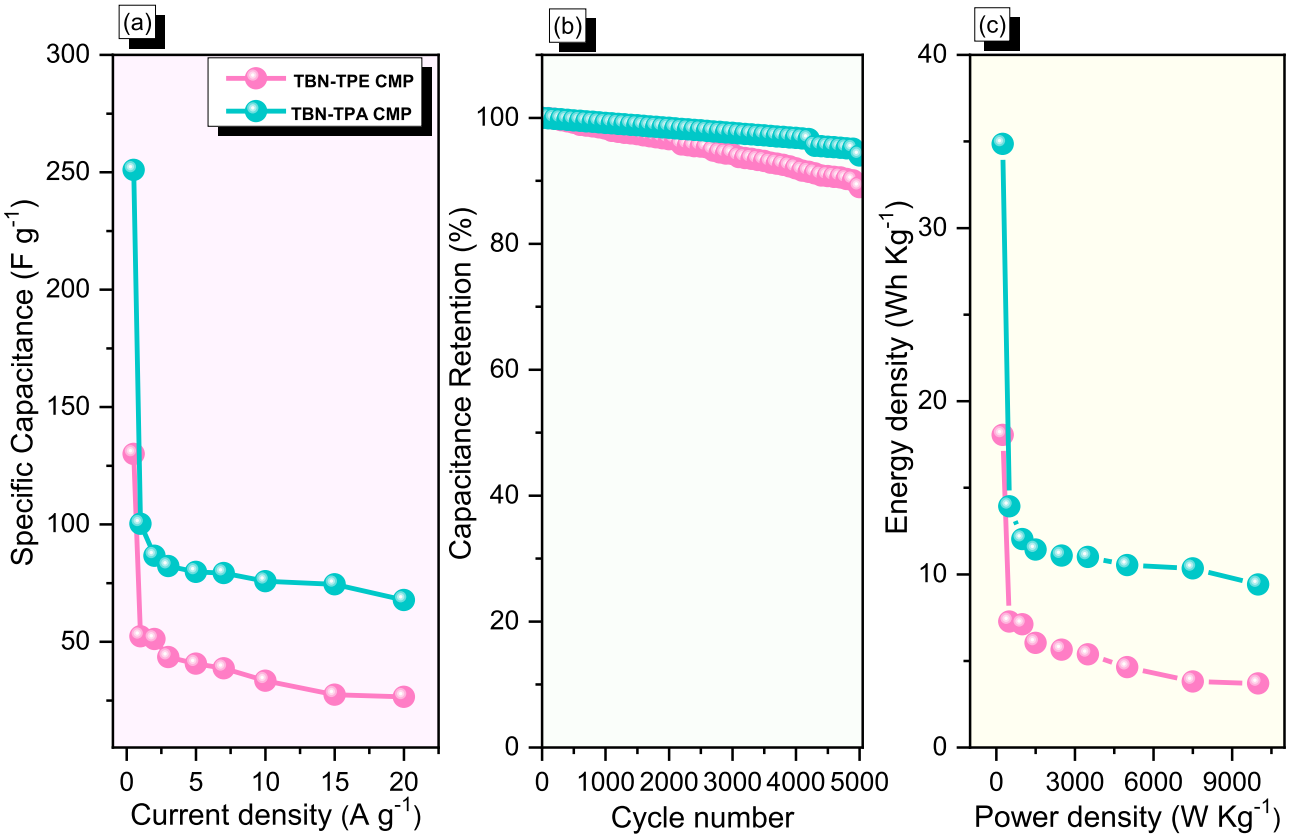

Fig. 4. (a) Specific capacitances, (b) cycling stability profiles, and (c) Ragone plots of the TBN-TPE and TBN-TPA CMPs.

electron microscopy (TEM) images of the TBN-TPE and TBN-TPA CMPs. The SEM images [Fig. 2(a)–(f)] of both samples revealed the presence of aggregated nanoparticles distributed throughout their surfaces. The corresponding TEM images [Fig. 2(g) and 2(h)] revealed the spherical morphologies of the two samples. SEM elemental mapping images of these CMPs identified the presence of C, N, and O atoms distributed on their surfaces (Figs. 2, S11, and S12).

3.1. *Three-Electrode electrochemical performance of the CMPs*

In an aqueous solution of KOH (1.0 M), both the TBN-TPE CMP and TBN-TPA CMPs electrochemical performance was evaluated using cyclic voltammetry (CV) and galvanostatic charge/discharge (GCD) profiles with the three-electrode system made up of glassy carbon, platinum, and Hg/HgO as the working, counter, and reference electrodes, respectively. Fig. 3(a) and 3(b) display the CV curves of the TBN-TPE and TBN-TPA CMPs, respectively, measured over the potential range from –1.0 to 0.0 V (vs Hg/HgO) using a wide range of scan rates (from 5 to 200 mV s^{-1}). The curves of both CMPs possessed characteristic rectangle-like humped shape, with redox peaks at −0.3 V and −0.5 V for TBN-TPE and TBN-TPA CMP respectively, and this shape has stayed constant with scan-sweeping, demonstrating that both of the obtained TBN—CMPs are stable concerning the current sweep and depict capacitance from EDLCs. The galvanostatic charge/discharge curves in which a nonlinearity arose revealed typical pseudo-capacitive behaviors of the samples, allowing for the observation of the redox processes. The redox peaks in the CV curves are connected with a minor variation in line slopes at around −0.3 V and −0.5 V for TBN-TPE and TBN-TPA CMP respectively [53]. Due to high surface areas and abundance of electrons from their phenyl groups, both CMPs exhibit high CV curve coherence across the range of scan rates. Furthermore, the abundance of heteroatoms and distinctive morphologies of these CMPs were responsible for their pseudocapacitance, with the CMPs experiencing high degrees of electron transfer through the formation of good contacts with the electrolyte. The CV curves also revealed the excellent rate capacities and straightforward kinetics of these CMPs. We examined the GCD patterns, and the capacitances of these materials at various current densities between 0.5 and 20 A g^{-1} [Fig. 3(c) and (d)]. All of the GCD curves featured a bowed-triangle form, suggesting a combination of pseudocapacitive and EDLC properties, presumably because of the presence of heteroatoms. Similar results for the coulombic efficiency (higher than 100%) [54–56], according to the physical definition, indicates that the system may be charged quickly and released gradually. This is due to the electrolyte ions' quick intercalation and surface diffusion during charging, and sluggish deintercalation during discharging, which implies that our TPA-CMP materials might be used as a potential hybrid battery-type supercapacitor. Fig. 4(a) presents the specific capacitance plots of our CMPs. The capacitances of the TBN-TPE and TBN-TPA CMPs were 130 and 251 F g^{-1}, respectively, measured at a current density of 0.5 A g^{-1}. We attribute the TBN-TPA CMP's remarkable performance to its chemical structure and high specific surface area (230 m^2 g^{-1}). The stacking of the benzene rings of its triphenylamine (TPA) moieties provided a structure suitable for high electrochemical activity and conductivity, due to electron dispersion, with its high porosity minimizing the effects of the electrolyte [57–60]. We investigated the cycling stabilities of our two CMPs over 5000 cycles at 10 A g^{-1} [Fig. 4(b)]. The capacity retention of the TBN-TPA CMP (94%) was higher than that of the TBN-TPECMP (89%). Even at high current densities, these compounds remained stable over extended cycling. In addition, the energy density of the TBN-TPA CMP (35 W h kg^{-1}) was extraordinary when compared with that of the TBN-TPE CMP (18 W h kg^{-1}) [Fig. 4(c)].

Further, the electric resistance provided by various electrodes via the ion diffusion process was investigated using electrochemical impedance spectroscopy. Fig. 5(a) displays several Nyquist plots, with identical fitted circuits, that allowed us to determine various features (e.g., series and charge transfer resistances) of the electrodes. In the presented fitting

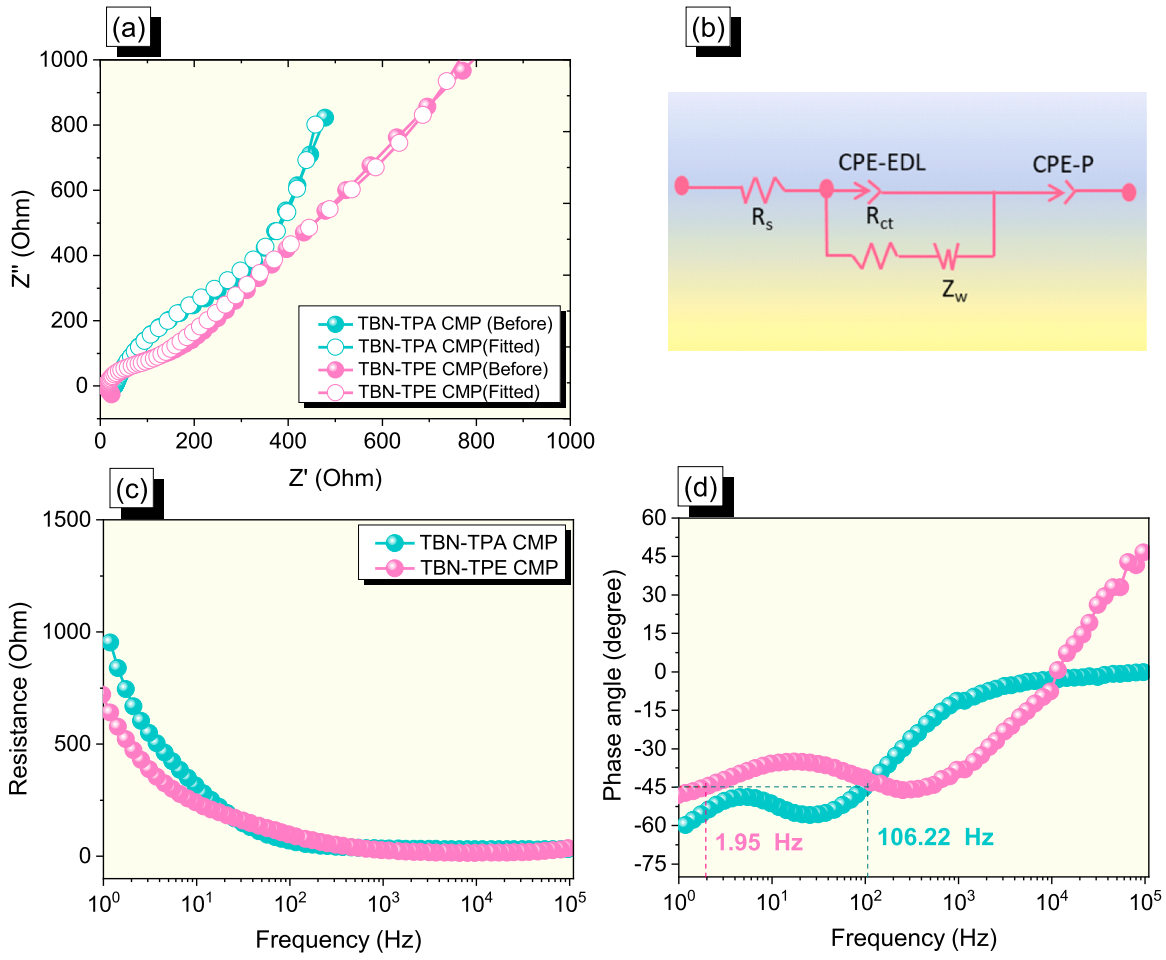

Fig. 5. (a) Nyquist plots, (b) fitted circuits, (c) Bode plots of the frequency with respect to the magnitude of resistance, and (d) Bode plots of the frequency with respect to phase angle to determine the knee frequency.

Table 2
Various parameters of the fitted Nyquist plots.

Sample	R_s (Ω)	R_{ct} (Ω)	CPE-EDL ($S.s^n$)	CPE-P ($S.s^n$)
TBN-TPA-CMP	30.83	429.5	0.0001159	0.0002052
TBN-TPE-CMP	15.49	75.1	0.0000112	0.0009756

circuit, the series and charge transfer resistances, the two constant phase elements, and the Warburg element are represented as R_s, R_{ct}, CPE-EDL, CPE-P, and Z_w, respectively [Fig. 5(b)]. According to Table 2, the initial series resistances (ohmic resistances) of the electrodes of the TBN-TPE and TBN-TPA CMPs were 15.49 and 30.83 Ω, respectively; their charge transfer resistances were 75.1 and 429.5 Ω, respectively. Even though the ohmic and charge transfer resistances of the TBN-TPECMP electrode were lower than those of the TBN-TPA CMP, both offered high specific capacities. Fig. 5(c) presents the frequency-dependent-magnitude Bode plots. The profiles feature slanted lines of negative slope at low frequencies and minimal resistances at higher frequencies, illustrating the excellent capacitive properties of these electrode materials. Fig. 5(d) displays the frequency-dependent phase angle charts for several electrodes. We calculated the knee frequencies from this figure for a phase angle of 45°, at which the electrodes' capacitive and resistive characteristics were identical. The knee frequencies of the TBN-TPE and TBN-TPA CMPs were 1.95 and 106.2 Hz, respectively. The rate performance is related to knee frequency; according to previous reports [61, 62], a greater rate performance is frequently linked to a higher knee frequency. We conclude that both the TBN-TPE and TBN-TPA CMPs demonstrated remarkable efficiency for use as electrode materials for energy storage.

In addition, we assembled CR2032 coin cells to assess the electrochemical performance of SSCs incorporating the TBN-TPE and TBN-TPA CMPs over the potential range from –0.7 to +0.3 V. We recorded the CV profiles of the TBN-TPE and TBN-TPA CMPs at various scan speeds between 5 and 200 mV s^{-1} [Fig. 6(a) and 6(b)]. All of the CV curves exhibited almost rectangular shapes, accompanied by humps in the lower potential region; this appearance is characteristic of SCs displaying both double-layer and pseudocapacitive properties. The integrity of the electrodes remained mostly intact upon increasing the scan rate, indicating a rise in current density and the greater rate capability, in addition to stability, of these electrode materials. Fig. 6(c) and 6(d) display the GCD profiles of the TBN-TPE and TBN-TPA CMP electrodes, respectively, measured at various current densities (1–10 A g^{-1}). The curves reveal the effects of both pseudocapacitance and electric double-layer capacitance; they are almost triangular, with an absent curve resulting from the heteroatoms in the CMP structures. At a current density of 1 A g^{-1}, the specific capacitances of the TBN-TPE and TBN-TPA CMP electrodes, determined from the GCD curves, were 20 and 32 F g^{-1}, respectively [Fig. 7(a)]. Thus, the capacitance of the TBN-TPA CMP electrode was higher than that of the TBN-TPE CMP, presumably because its higher surface area facilitated ion mobility, thereby boosting the rate capability and stability of the electrode, leading to the material's exceptional performance. In addition, we tested the cycling stability of the CMPs over 5000 cycles at 10 A g^{-1} [Fig. 7(b)]. The capacity retention of the TBN-TPA CMP (90%) was higher than that of the TBN-TPE CMP (85%). Furthermore, the energy density of the TBN-TPE CMP

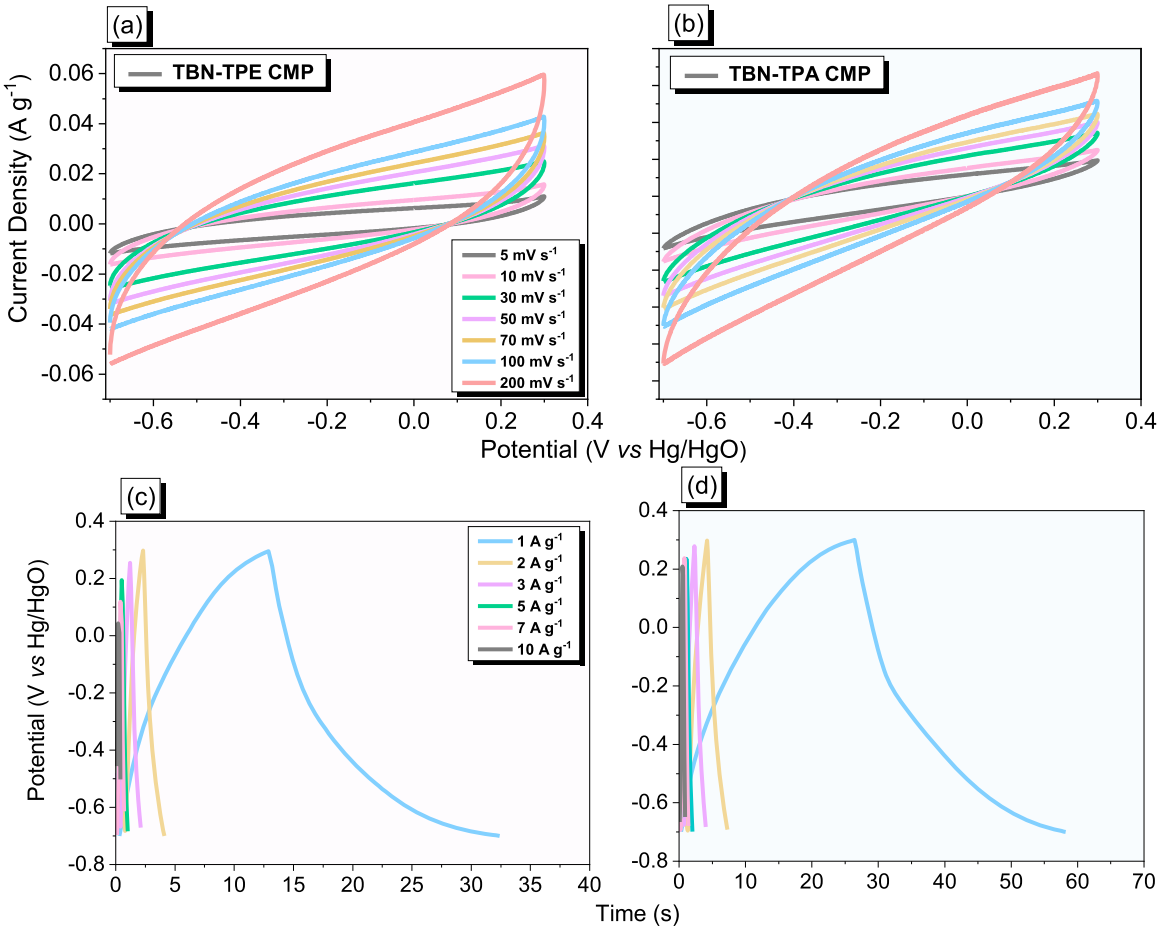

Fig. 6. (a, b) CV and (c, d) curves of SSC coin cells incorporating the (a, c) TBN-TPE and (b, d) TBN-TPA CMPs.

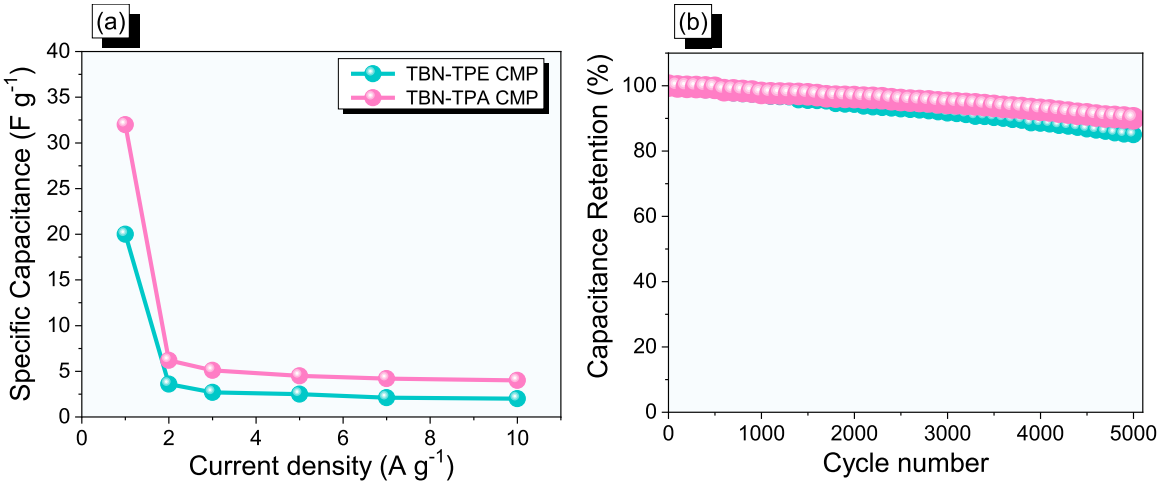

Fig. 7. (a) Specific capacitances, and (b) long cycling stability profiles of SSC coin cells incorporating the TBN-TPE and TBN-TPA CMPs.

(3 W h kg^{-1}) was slightly lower than that of the TBN-TPA CMP (5 W h kg^{-1}) [Fig. S13]. Fig. S14 presents a photograph of a bright LED powered by a TBN-TPA CMP–containing an SSC coin cell.

4. Conclusion

We have prepared two tetrabenzonaphthalene-linked CMPs—the TBN-TPE and TBN-TPA CMPs, with specific surface areas of 126 and 230 m^2 g^{-1}, respectively—through facile Schiff-base condensations. The TBN-TPA CMP, comprising tetrabenzonaphthalene and TPA moieties, appears to be a suitable electrode material for energy storage applications, because its chemical structure, effective porosity, and stacking of benzene rings in its redox-active TPA units led to high electrochemical activity and high conductivity. The TBN-TPA CMP presented outstanding specific capacitances of 251 F g^{-1} (at 0.5 A g^{-1}) and 32 F g^{-1} (at a current of 1 A g^{-1}), along with high-capacity retentions of 94 and 90% after 5000 cycles at 10 A g^{-1}, when measured in both three-electrode and two-electrode SSC devices, respectively. These findings

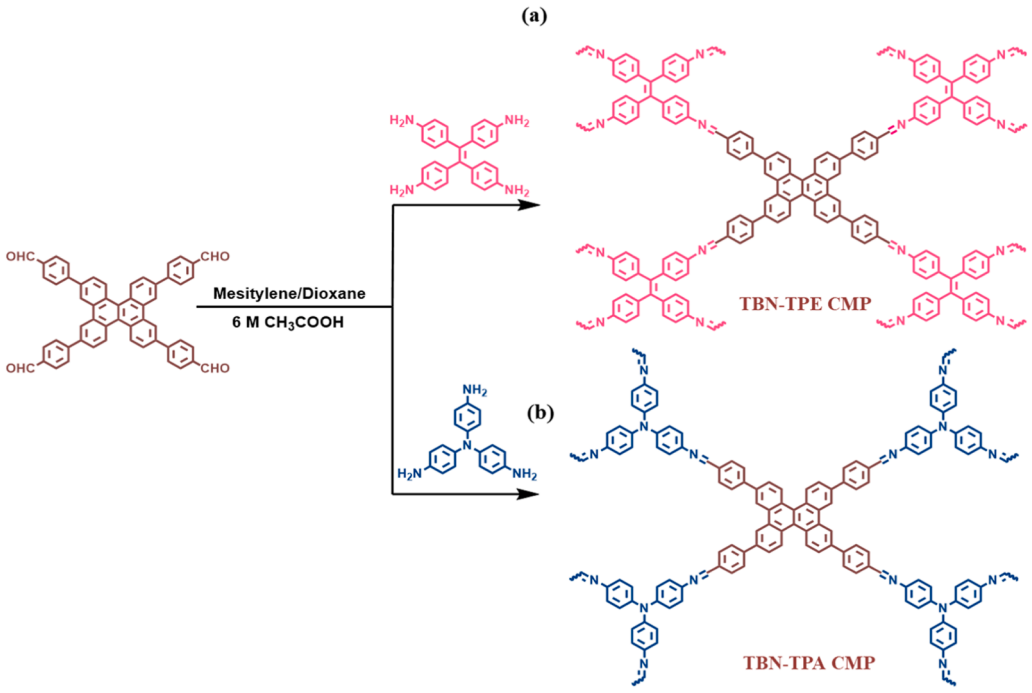

Scheme 1. Synthesis of the (a) TBN-TPE and (b) TBN-TPA CMPs.

suggest that it will be possible to design highly efficient electroactive materials for applications in energy storage systems, batteries, and other electrochemical devices.

Declaration of Competing Interest

The authors declare that they have no known competing financial interests or personal relationships that could have appeared to influence the work reported in this paper.

Acknowledgments

This study was supported financially by the Ministry of Science and Technology, Taiwan, under contracts NSTC 110–2124-M-002–013 and 111–2223-E-110–004. The authors thank the staff at National Sun Yat-sen University for their assistance with the TEM (ID: EM022600) experiments.

Supplementary materials

Supplementary material associated with this article can be found, in the online version, at doi:10.1016/j.jtice.2023.104750.

References

[1] Ejaz M, Samy MM, Ye Y, Kuo SW, Mohamed MG. Design hybrid porous organic/inorganic polymers containing polyhedral oligomeric Silsesquioxane/Pyrene/Anthracene moieties as a high-performance electrode for supercapacitor. Int J Mol Sci 2023;24:2501.
[2] Liao Y, Wang H, Zhu M, Thomas A. Efficient supercapacitor energy storage using conjugated microporous polymer networks synthesized from buchwald–Hartwig coupling. Adv Mater 2018;30:1705710.
[3] Loganathan NN, Perumal V, Pandian BR, Atchudan R, Edison TNJI, Ovinis M. Recent studies on polymeric materials for supercapacitor development. J Energy Storage 2022;49:104149.
[4] Samy MM, Mohamed MG, El-Mahdy AFM, Mansoure TH, Wu KCW, Kuo SW. High-performance supercapacitor electrodes prepared from dispersions of tetrabenzonaphthalene-based conjugated microporous polymers and carbon nanotubes. ACS Appl Mater Interfaces 2021;13:51906–16.
[5] Zheng S, Li Q, Xue H, Pang H, Xu Q. A highly alkaline stable metal oxide@metal-organic framework composite for high performance electrochemical energy storage. Natl Sci Rev 2020;7:305–14.
[6] Liu C, Bai Y, Li W, Yang F, Zhang G, Pang HIn. Situ Growth of Three-Dimensional MXene/Metal-Organic Framework Composites for High-Performance Supercapacitors. Angew Chem, Int Ed 2022;61:e202116282.
[7] Liu S, Kang L, Henzie J, Zhang J, Ha J, Amin MA, Hossain MSA, Jun SC, Yamauchi Y. Recent advances and perspectives of battery-type anode materials for potassium ion storage. ACS Nano 2021;15:18931–73.
[8] Liu S, Kang L, Zhang J, Jung E, Lee S, Jun SC. Structural engineering and surface modification of MOF-derived cobalt-based hybrid nanosheets for flexible solid-state supercapacitors. Energy Storage Mater 2020;32:167–77.
[9] Chen WC, Liu YT, Kuo SW. Mesoporous organic/inorganic hybrid materials with frank-kasper phases templated by an unusual linear symmetry diblock copolymer. Macromol Rapid Commun 2021;42:2100302.
[10] Liu S, Kang L, Zhang J, Jun SC, Yamauchi Y. Carbonaceous anode materials for non-aqueous sodium- and potassium-ion hybrid capacitors. ACS Energy Lett 2021;6:4127–54.
[11] Xu Z, Sun S, Han Y, Wei Z, Cheng Y, Yin S, Cui W. High energy-density asymmetric supercapacitor based on a durable and stable manganese molybdate nanostructure electrode for energy storage systems. Appl. Energy Mater. 2020;3:5393–404.
[12] Liu S, Kang L, Hu J, Jung E, Zhang J, Jun SC, Yamauchi Y. Unlocking the potential of oxygen-deficient copper-doped Co_3O_4 nanocrystals confined in carbon as an advanced electrode for flexible solid-state supercapacitors. ACS Energy Lett 2021;6:3011–9.
[13] Mohamed MG, Samy MM, Mansoure TH, Li CJ, Li WC, Chen JH, Zhang K, Kuo SW. Microporous carbon and carbon/metal composite materials derived from bio-benzoxazine-linked precursor for CO_2 capture and energy storage applications. Int J Mol Sci 2022;23:347. https://doi.org/10.3390/ijms23010347.
[14] Borenstein A, Hanna O, Attias R, Luski S, Brousse T, Aurbach D. Carbon-based composite materials for supercapacitor electrodes: a review. J Mater Chem A 2017;5:12653–72.
[15] Dong Y, Zhu J, Li Q, Zhang S, Song H, Jia D. Carbon materials for high mass-loading supercapacitors: filling the gap between new materials and practical applications. J Mater Chem A 2020;8:21930–46.
[16] Simon P, Gogotsi Y. Materials for electrochemical capacitors. Nat Mater 2008;7:845–54.
[17] Wang YG, Li HQ, Xia YY. Ordered Whiskerlike polyaniline grown on the surface of mesoporous carbon and its electrochemical capacitance performance. Adv Mater 2006;18:2619–23.
[18] Zhang LL, Zhao XS. Carbon-based materials as supercapacitor electrodes. Chem Soc Rev 2009;38:2520–31.
[19] Zhou Y, Qin ZY, Li L, Zhang Y, Wei YL, Wang LF, Zhu MF. Polyaniline/multi-walled carbon nanotube composites with core–shell structures as supercapacitor electrode materials. Electrochim Acta 2010;55:3904.
[20] Liao Y, Cheng Z, Trunk M, Thomas A. Targeted control over the porosities and functionalities of conjugated microporous Polycarbazole networks for CO_2-selective capture and H_2 storage. Polym Chem 2017;8:7240–7.
[21] Lee JSM, Cooper AI. Advances in conjugated microporous polymers. Chem Rev 2020;120:2171–214.
[22] Lyu W, Zhang W, Liu H, Liu Y, Zuo H, Yan C, Faul CFJ, Thomas A, Zhu M, Liao Y. Conjugated microporous polymer network grafted carbon nanotube fibers with

tunable redox activity for efficient flexible wearable energy storage. Chem Mater 2020;32:8276–85.
[23] Amin K, Ashraf N, Mao L, Faul CFJ, Wei Z. Conjugated microporous polymers for energy storage: recent progress and challenges. Nano Energy 2021;85:105958.
[24] Kou Y, Xu Y, Guo Z, Jiang D. Supercapacitive energy storage and electric power supply using an aza-fused π-conjugated microporous framework. Angew Chem Int Ed 2011;123:8912–6.
[25] Xu M, Zhang S, Wang T, Yu B, Yang Z, Wang X, Zhou R, Hua D. De novo design of a Pt Nanocatalyst on a conjugated microporous polymer-coated honeycomb carrier for oxidation of hydrogen isotopes. ACS Appl Mater Interfaces 2022;14:7826–35.
[26] Thomas A, Kuhn P, Weber J, Titirici MM, Antonietti M. Porous polymers: enabling solutions for energy applications. Macromol Rapid Commun 2009;30:221–36.
[27] Jiang JX, Wang C, Laybourn A, Hasell T, Clowes R, Khimyak YZ, Xiao J, Higgins SJ, Adams DJ, Cooper AI. Metal-organic conjugated microporous polymers. Angew Chem, Int Ed 2011;50:1072–5.
[28] Samy MM, Sharma SU, Mohamed MG, Mohammed AAK, Chaganti SV, Lee JT, Kuo SW. Conjugated microporous polymers containing ferrocene units for high carbon dioxide uptake and energy storage. Mater Chem Phys 2022;287:126177.
[29] Mohamed MG, Chang WC, Kuo SW. Crown ether- and Benzoxazine-linked porous organic polymers displaying enhanced metal ion and CO_2 capture through solid-state chemical transformation. Macromolecules 2022;55:7879–92.
[30] Mohamed MG, Hu HY, Madhu M, Ejaz M, Sharma SU, Tseng WL, Samy MM, Huang CW, Lee JT, Kuo SW. Construction of ultrastable conjugated microporous polymers containing thiophene and fluorene for metal ion sensing and energy storage. Micromachines (Basel) 2022;13:1466. https://doi.org/10.3390/mi13091466.
[31] Mohamed MG, Mansour TH, Takashi Y, Samy MM, Chen T, Ku SW. Ultrastable porous organic/inorganic polymers based on polyhedral oligomeric silsesquioxane (POSS) hybrids exhibiting high performance for thermal property and energy storage. Microporous Mesoporous Mater 2021;328:111505.
[32] Zhu Z, Yan Z, Fan Y, Liu C, Sun H, Liang W, Li A. Calcination of porphyrin-based conjugated microporous polymers nanotubes as nanoporous N-Rich Metal-Free Electrocatalysts for efficient oxygen reduction reaction. ACS Appl Energy Mater 2020;3:5260–8.
[33] Shu L, Yu J, Cui Y, Ma Y, Li Y, Gao B, Wang HG. Porphyrin-based conjugated microporous polymers with dual active sites as anode materials for lithium-organic batteries. Int J Hydrog Energy 2022;47:10902–10.
[34] Wang X, Maeda K, Thomas A, Takanabe K, Xin G, Carlsson JM, Domen K, Antonietti M. A metal-free polymeric photocatalyst for hydrogen production from water under visible light. Nat Mater 2009;8:76–80.
[35] Chen L, Honsho Y, Seki S, Jiang D. Light-harvesting conjugated microporous polymers: rapid and highly efficient flow of light energy with a porous polyphenylene framework as antenna. J Am Chem Soc 2010;132:6742–8.
[36] Thomas A. Functional materials: from hard to soft porous frameworks. Angew Chem, Int Ed 2010;49:8328–44.
[37] Mohamed MG, Sharma SU, Yang CH, Samy MM, Mohammed AAK, Chaganti SV, Lee JT, Kuo SW. Anthraquinone-enriched conjugated microporous polymers as organic cathode materials for high-performance lithium-ion batteries. ACS Appl Energy Mater 2021;4:14628–39.
[38] Xie Z, Wang C, DeKrafft KE, Lin W. Highly stable and porous cross-linked polymers for efficient photocatalysis. J Am Chem Soc 2011;133:2056–9.
[39] Ju P, Qi W, Guo B, Liu W, Wu Q, Su Q. Highly Stable and Versatile Conjugated Microporous Polymer for Heterogeneous Catalytic Applications. Catal Lett 2022. https://doi.org/10.1007/s10562-022-04131-y.
[40] Ren L, Geng T. Tetraphenylethylene-based fluorescent conjugated microporous polymers for fluorescent sensing trinitrophenol. Bull Mater Sci 2022;45:137.
[41] Bezzu CG, Carta M, Tonkins A, Jansen JC, Bernardo P, Bazzarelli F, McKeown NB. A spirobifluorene-based polymer of intrinsic microporosity with improved performance for gas separation. Adv Mater 2012;24:5930–3.
[42] Mohamed MG, Atayde ECJ, Matsagar BM, Na J, Yamauchi Y, Wu KCW, Kuo SW. Construction hierarchically mesoporous/microporous materials based on block copolymer and covalent organic framework. J Taiwan Inst Chem Eng 2020;112:180–92.
[43] Wei Z, Wang D, Liu Y, Guo X, Zhu Y, Meng Z, ZQ Y, Wong WY. Ferrocene-based hyperbranched polymers: a synthetic strategy for shape control and applications as electroactive materials and precursor-derived magnetic ceramics. J Mater Chem C 2020;8:10774–80.
[44] Du N, Park HB, Robertson GP, Dal-Cin MM, Visser T, Scoles L, Guiver MD. Polymer nanosieve membranes for CO_2- capture applications. Nat Mater 2011;10:372–5.
[45] Samy MM, Mekhemer IMA, Mohamed MG, Elsayed MH, Lin KH, Chen YK, Wu TL, Chou HH, Kuo SW. Conjugated microporous polymers incorporating Thiazolo[5,4-*d*]thiazole moieties for Sunlight-Driven hydrogen production from water. Chem Eng J 2022;446:137158.
[46] Baumann AE, Burns DA, Liu B, Thoi VS. Metal-organic framework functionalization and design strategies for advanced electrochemical energy storage devices. Commun Chem 2019;2:86.
[47] Eftekhari A, Fang B. Electrochemical hydrogen storage: opportunities for fuel storage, batteries, fuel cells, and supercapacitors. Int J Hydrogen Energy 2017;42:25143–65.
[48] Mehtab T, Yasin G, Arif M, Shakeel M, Korai RM, Nadeem M, Muhammad N, Lu X. Metal-organic frameworks for energy storage devices: batteries and supercapacitors. J Energy Storage 2019;21:632–46.
[49] Li Y, Wang G, Wei T, Fan Z, Yan P. Nitrogen and sulfur co-doped porous carbon nanosheets derived from willow catkin for supercapacitors. Nano energy 2016;19:165–75.
[50] Mohamed MG, Samy MM, Mansoure TH, Sharm SU, Tsai MS, Chen JH, Lee JT, Kuo SW. Dispersions of 1,3,4-oxadiazole-linked conjugated microporous polymers with carbon nanotubes as a high-performance electrode for supercapacitors. ACS Appl Energy Mater. 2022;5:3677–88.
[51] Mohamed MG, Lee CC, EL-Mahdy AFM, Lüder J, Yu MH, Li Z, Zhu Z, Chueh CC, Kuo SW. Exploitation of two-dimensional conjugated covalent organic frameworks based on tetraphenylethylene with bicarbazole and pyrene units and applications in perovskite solar cells. J Mater Chem A 2020;8:11448–59.
[52] Lin RC, Mohamed MG, Kuo SW. Benzoxazine/Triphenylamine-Based Dendrimers Prepared through Facile One-Pot Mannich Condensations. Macromol Rapid Commun 2017;38:1700251.
[53] Zhou J, Lian J, Hou L, Zhang J, Gou H, Xia M, Zhao Y, Strobel TA, Lu Tao L, Gao F. Ultrahigh volumetric capacitance and cyclic stability of fluorine and nitrogen co-doped carbon microspheres. Nat Commun 2015;6:8503. https://doi.org/10.1038/ncomms9503. 6.
[54] Wang Q, Zhang Y, Jiang H, Hu T, Meng C. In situ generated $Ni_3Si_2O_5(OH)_4$ on mesoporous heteroatom-enriched carbon derived from natural bamboo leaves for high-performance supercapacitors. ACS Appl. Energy Mater. 2018;1:3396–409. https://doi.org/10.1021/acsaem.8b00556.
[55] Xu Z, Sun S, Han Y, Wei Z, Cheng Y, Shougen Yin S, Cui W. High-energy-density asymmetric supercapacitor based on a durable and stable manganese molybdate nanostructure electrode for energy storage systems. ACS Appl. Energy Mater. 2020;3:5393–404. https://doi.org/10.1021/acsaem.0c00393.
[56] Bhattacharya G, Fishlock SJ, Roy JS, Pritam A, Banerjee D, Deshmukh S, Ghosh S, McLaughlin JA, Susanta Roy SS. Effective utilization of waste red mud for high performance supercapacitor electrodes. Global Challenges 2019;3:1800066. https://doi.org/10.1002/gch2.201800066.
[57] Samy MM, Mohamed MG, Sharma SU, Chaganti SV, Mansoure TH, Lee JT, et al. Constructing conjugated microporous polymers containing triphenylamine moieties for high-performance capacitive energy storage. Polymer 2023;264:125541.
[58] Su C, He H, Xu L, Zhao K, Zheng C, Zhang C. A mesoporous conjugated polymer based on a high free radical density polytriphenylamine derivative: its preparation and electrochemical performance as a cathode material for Li-ion batteries. J Mater Chem A 2017;5:2701.
[59] Weng TH, Mohamed MG, Sharma SU, Chaganti SV, Samy MM, Lee JT, Kuo SW. Ultrastable Three-Dimensional Triptycene- and Tetraphenylethene-conjugated microporous polymers for energy storage. ACS Appl. Energy Mater. 2022;5:14239–49.
[60] Mohamed MG, Elsayed MH, Ye Y, Samy MM, Ahmed AE, Hassan TH, et al. Construction of porous Organic/Inorganic hybrid polymers based on polyhedral oligomeric silsesquioxane for energy storage and hydrogen production from water. Polymers (Basel) 2023;15:182. https://doi.org/10.3390/polym15010182.
[61] Mohamed MG, Sharma SU, Liu NY, Mansour TH, Sam MM, Chaganti SV, Chang YL, Lee JT, Kuo SW. Ultrastable covalent triazine organic framework based on anthracene moiety as platform for high-performance carbon dioxide adsorption and supercapacitors. Int J Mol Sci 2022;23:3174. https://doi.org/10.3390/ijms23063174.
[62] Lyu W, Yan C, Chen Z, Chen J, Zuo H, Teng L, Liu H, Wang L, Liao Y. Spirobifluorene-based conjugated microporous polymer-grafted carbon nanotubes for efficient Supercapacitive energy storage. ACS Appl Energy Mater 2022;5:3706–14.